Combustion and Flame xxx (2014) xxx–xxx

Contents lists available at ScienceDirect

Combustion and Flame

journal homepage: www.elsevier.com/locate/combustflame

A comparison of various models in predicting ignition delay in single-particle coal combustion

Babak Goshayeshi, James C. Sutherland *

The University of Utah, Department of Chemical Engineering, United States

ARTICLE INFO

Article history:
Received 19 July 2013
Received in revised form 5 November 2013
Accepted 7 January 2014
Available online xxxx

Keywords:
Coal
Devolatilization
Ignition delay

ABSTRACT

In this paper, individual coal particle combustion under laminar conditions is simulated using models with various levels of complexity for the particle and gas phase chemical kinetics. The mass, momentum and energy governing equations are fully coupled between the particle and the gas phase. In the gas phase, detailed chemical kinetics based on GRI3.0 and infinitely-fast chemistry are considered and compared. For the particle phase, models for vaporization, devolatilization and char oxidation/gasification are considered, and the Kobayashi–Sarofim devolatilization model is compared to the Chemical Percolation Devolatilization (CPD) model. Ignition delay is used as a quantitative metric to compare the simulation prediction with experimental data, with careful attention given to the definition of ignition delay in the simulations. The effects of particle size, coal type and gas-phase temperature on the ignition delay are studied and compared with experimental data.

1. Introduction

Coal combustion/gasification is a complex process with many coupled sub-processes occurring simultaneously [1]. Furthermore, most practical coal combustion systems are turbulent, further complicating the modeling challenge because of the nonlinear coupling occurring across a multitude of length and time scales. Even with modern day computers, resolving the entire physics of the problem remains prohibitively expensive. Coal combustion/gasification models must address particle dynamics in turbulent flow, gas-phase thermochemistry, heterogeneous reactions between the coal and gas, devolatilization/pyrolysis, vaporization, radiative heat transfer, *etc.*

The modeling challenge for coal combustion is further complicated by the varying properties and chemical structure of different coal types [2], and by the fact that the coal properties change significantly throughout a coal particle's lifetime in a combustor [3–5]. The coal particle thermochemistry in this work is divided into three processes: vaporization, devolatilization and char oxidation/gasification.

Models for devolatilization vary widely in complexity, with the most sophisticated models accounting for the chemical structure of the coal and its effect on the devolatilization process [1]. In 1971, a constant value was proposed for the combustion rate of each coal type [6]. Arrhenius-form models such as the single-rate [7] and Kobayashi [8] models describe devolatilization with a kinetic rate. In 1976, the Distributed Activation Energy (DAE) model [9] proposed using a Gaussian distribution for the activation energy. Determining the parameters for the Gaussian distribution were the challenges of this model [10]. Representing coal as a collection of functional group including aromatic rings, aliphatic chains and bridges and oxygen-carrying groups was a significant step in devolatilization modeling [11,12]. The Chemical Percolation Devolatilization (CPD) model accounts for the thermal decomposition of the macromolecular network and accounts for structural variation among various coal types [13,14,1], and can accurately describe light-gas evolution from coal devolatilization [15]. In this work, the Kobayashi and CPD devolatilization models (representing a relatively simple and fairly sophisticated model, respectively) are utilized; their ability to predict ignition delay are examined.

Char oxidation and gasification are heterogenous reactions, and are significantly slower than the vaporization and devolatilization processes [1,16]. There are many factors influence the char oxidation, such as coal structure, coal type, the gas-phase environment (*e.g.*, oxygen partial pressure) and temperature [17,18]. The products of char oxidation are mainly carbon dioxide and monoxide [19,20]. A common assumption in coal combustion modeling is that char oxidation occurs after the coal particle is fully devolatilized [21,22]. The present study and formulation allow for simultaneous vaporization, devolatilization and char oxidation and do not impose any temporal ordering/sequencing of these processes.

The influence of systems parameters such as oxidizer composition and coal rank on ignition delay and flame stability have been explored experimentally by several researchers [23–29]. A review on experiments measuring the coal particle ignition delay is

* Corresponding author.
E-mail address: James.Sutherland@utah.edu (J.C. Sutherland).

0010-2180/$ - see front matter © 2014 The Combustion Institute. Published by Elsevier Inc. All rights reserved.
http://dx.doi.org/10.1016/j.combustflame.2014.01.010

reported in [30]. In [25], the influence of gas phase temperature and particle size on the single particle ignition delay are also considered as parameters. In this work, the ignition delay is employed as metric to evaluate simulation results where the effect of gas phase temperature, coal rank and particle size on ignition delay are studied and compared to the experiments conducted by [25].

Although numerous simulations of coal combustion have been performed, most use relatively simple models for the devolatilization and gas-phase combustion process [31–35]. The flamelet and flame-sheet models are used in simulation of single coal particle combustion by different groups [36,34,31]. Attempts to address limitations of these models have used two- and four-step global mechanisms [26]. Hecht et al. performed one-dimensional simulations on char oxidation of single coal particles with detailed kinetics to determine the temperature and species radial profiles for char oxidation, but used boundary-layer assumptions to treat diffusion [37–39].

The objective of this work is to evaluate the efficacy of devolatilization and gas-phase chemistry models for coal combustion/gasification. To this end, we compare experimental observations of coal particle ignition delay to two devolatilization models paired with two gas-phase kinetics models. To the authors' knowledge, this is the first computational study examining ignition delay using detailed kinetics in the gas phase fully coupled to a high-fidelity model (CPD) for devolatilization of coal particles. We consider the effect of key parameters including particle size, furnace temperature, and coal type on the ignition delay time, and evaluate a few simplified modeling strategies relative to the detailed models and experimental data.

This paper is organized as follows: the governing equations are described in Section 2. Section 3 then provides a description of the models for gas-phase kinetics and coal particles (including evaporation, devolatilization, char oxidation/gasification). The simulation results, including trends with varying the reactor temperature and particle sizes, are discussed in Section 5, and compared to experimental ignition delay data.

2. Governing equations

The governing equations for gas and particle phase are provided in this section. A one-dimensional domain aligned with the y-coordinate that evolves in time was considered in this work.

2.1. Gas phase

The gas-phase equations are solved in an Eulerian frame of reference. The overall mass conservation equation in the gas phase is

$$\frac{\partial \rho}{\partial t} = -\frac{\partial v}{\partial y} + \sum_{j=1}^{n_p} S_{p_j m}, \tag{1}$$

where ρ is the gas phase density, v is the gas velocity at y direction (lateral), $S_{p_j m}$ is the particle source term accounting for interphase mass exchange and n_p is the total number of particles (in this work, simulations are performed for a single particle). Individual species conservation equations accounting for interphase mass exchange are given as

$$\frac{\partial \rho Y_i}{\partial t} = -\frac{\partial \rho Y_i v}{\partial y} - \frac{\partial J_i}{\partial y} + \omega_i + \sum_{j=1}^{n_p} S_{p_j Y_i}, \tag{2}$$

where Y_i, J_i and ω_i are the mass fraction, mass-diffusive flux and reaction source term of species i, respectively, and $S_{p_j Y_i}$ is the release rate of species i from particle j into the gas phase.

Momentum equations are evolved for the component of momentum aligned with the resolved (y) direction and one orthogonal component,

$$\frac{\partial \rho v}{\partial t} = -\frac{\partial \rho v v}{\partial y} - \frac{\partial \tau_{yy}}{\partial y} - \frac{\partial P}{\partial y} + \sum_{j=1}^{n_p} S_{p_j v}, \tag{3}$$

$$\frac{\partial \rho u}{\partial t} = -\frac{\partial \rho v u}{\partial y} - \frac{\partial \tau_{yx}}{\partial y} + \sum_{j=1}^{n_p} S_{p_j u}. \tag{4}$$

where v and u refer to lateral and streamwise velocities, respectively. Finally, the energy equation is

$$\frac{\partial \rho e_0}{\partial t} = -\frac{\partial \rho e_0 v}{\partial y} - \frac{\partial p v}{\partial y} - \frac{\partial \tau_{yy} v}{\partial y} - \frac{\partial q}{\partial y} + \sum_{j=1}^{n_p} S_{p_j e_0}, \tag{5}$$

where e_0 is the internal energy and q is the heat diffusive flux. Closure of this system is achieved by the ideal gas equation of state, $P = \rho RT/M$ and constitutive relationships for the diffusive fluxes [40]

$$\tau_{yy} = -\frac{4}{3}\mu \frac{\partial v}{\partial y}, \tag{6}$$

$$\tau_{yx} = -\mu \frac{\partial u}{\partial y}, \tag{7}$$

$$q = -\kappa \frac{\partial T}{\partial y} + \sum_{i=1}^{n_s} h_i J_i, \tag{8}$$

$$J_i = -\frac{\rho Y_i}{X_i} D_i^{mix} \frac{\partial X_i}{\partial y}, \tag{9}$$

where μ is the viscosity, κ is the thermal conductivity, h_i is the species enthalpy, X_i is a species mole fraction, D_i^{mix} is the species mixture-averaged diffusivity and n_s is the number of species. Here, μ, κ and D_i^{mix} are functions of temperature, pressure and composition. Finally, temperature is obtained from the internal energy via a Newton-solve that incorporates the variation in composition and pressure.

The source terms S_{pm}, S_{pv}, S_{pu}, S_{pe_0} and S_{pY_i}, which account for interphase heat, mass and momentum transfer, will be described in Section 2.3. Corresponding exchange terms are included in the particle phase governing equations.

Additional models can be incorporated to include the effects of turbulent mixing [41,40]. For the purposes of this paper, only laminar flow is considered to isolate the effects of the thermochemical models from the turbulence models. Further discussion and derivation of the gas-phase governing equations can be found in [40,42].

2.2. Particle phase

Particles are transported in a Lagrangian frame of reference where each particle's position, velocity, mass, and thermochemical state are evolved. Although they have mass and volume, it is assumed that the particles do not displace fluid on the Eulerian mesh where the gas-phase equations are solved. Rather, particle source terms are interpolated onto the mesh and gas-phase quantities are interpolated to the particle location for purposes of interphase coupling. This assumption is reasonable provided that the gas phase mesh spacing is large relative to the particle size, which is the case for the simulations performed here. The motion of a single particle in gas–solid flows can be described by using Newton's second law

$$m_p \frac{du_{i,p}}{dt} = m_p g_i + S_{p_j,v} + F_c, \tag{10}$$

where i denotes the ith direction, m_p, $u_{i,p}$, g_i, $S_{p_j,v}$, and F_c are mass of single particle, particle velocity, gravity acceleration in ith direction, force generated by fluid–particle interaction, and force

generated by particle–particle interaction. For this study, particle–particle interaction is ($F_c = 0$) and the drag force is described by Stokes' law so that the particle momentum equations become

$$\frac{du_{p_j}}{dt} = \frac{g_i(\rho_p - \rho_g)}{\rho_p} + S_{p_j,u}, \tag{11}$$

$$\frac{dv_{p_j}}{dt} = \frac{g_i(\rho_p - \rho_g)}{\rho_p} + S_{p_j,v}. \tag{12}$$

Particle source terms for v ($S_{p_j,v}$) and u ($S_{p_j,u}$) are given by (16) and (17), respectively.

Given the evolution of the particle velocity according to (11) and (12), the particle position evolves as

$$\frac{dx_{i,p}}{dt} = u_{i,p}, \tag{13}$$

where $x_{i,p}$ is particle location in ith direction.

The particle energy evolution is given by

$$\frac{dT_p}{dt} = \frac{-A_p}{m_p C_p}[h_c(T_p - T) + \varepsilon\sigma(T_p^4 - T_w^4)] + S_r, \tag{14}$$

where T_p, T_w and T are the particle, wall, and gas temperatures respectively. C_p, m_p, A_p and ϵ are the particle heat capacity, mass, surface area (sphere surface) and emissivity respectively, σ is the Stefan–Boltzmann constant, $h_c = Nu\kappa/d_p$ is the convective heat transfer coefficient with $Nu = 2.0 + 0.6Re_p^{1/2}Pr^{1/3}$ [43] where d_p is the particle diameter, and S_r is the temperature source term due to vaporization and heterogeneous reactions defined by (21). In this work, radiation is considered only between particles and an "effective" furnace environment.

The overall mass balance on coal particle (m_p) is divided into three phenomenological categories describing the evolution of moisture (m_{H_2O}), volatiles (m_v), and char (m_c),

$$\frac{dm_p}{dt} = \frac{dm_{H_2O}}{dt} + \frac{dm_v}{dt} + \frac{dm_c}{dt}. \tag{15}$$

2.3. Source terms

The momentum exchange terms which appear in the gas and particle momentum balances are

$$S_{pv} = -\frac{m_p f_d}{\tau_p V_{cell}}(v - v_p), \tag{16}$$

$$S_{pu} = -\frac{m_p f_d}{\tau_p V_{cell}}(u - u_p), \tag{17}$$

where $\tau_p = \frac{d_p^2}{18\nu_g}$ is the particle relaxation time [44], f_d is the drag force coefficient and V_{cell} is a scaling term representing the volume of the control volume, respectively. The model employed for f_d is

$$f_d = \begin{cases} 1 & Re_p < 1 \\ 1 + 0.15Re_p^{0.687} & 1 < Re_p < 1000 \\ 0.0183Re_p & Re_p > 1000 \end{cases},$$

where

$$Re_p = \frac{d_p|u_p - u_g|}{\nu_g} \tag{18}$$

is the particle Reynolds number and ν_g is the gas kinematic viscosity. Subscripts p and g indicate particle and gas phase properties, respectively.

Most of the particle mass (except ash) is released to the gas phase during the combustion process. Furthermore, char oxidation and gasification requires additional species from the gas phase such as oxygen and carbon monoxide. The mass source term for single particle for species i can be written as

$$S_{pY_i} = \left(\frac{dm_i}{dt}\right)^{Evap} + \left(\frac{dm_i}{dt}\right)^{Dev} + \left(\frac{dm_i}{dt}\right)^{Oxid} + \left(\frac{dm_i}{dt}\right)^{Gasif}. \tag{19}$$

Models for evaporation, devolatilization, and char oxidation/gasification in (19) will be discussed in Section 3.2.

The energy source term for the gas phase energy conservation equation, (5), is given as

$$S_{pe_0} = \alpha\left(S_{p,CO}\Delta H_{CO} + S_{p,CO_2}\Delta H_{CO_2}\right)^{Oxid} + \alpha\left(\frac{dm_c}{dt}\right)_{H_2O}\Delta H_{H_2O}^{Gasif} + \alpha\left(\frac{dm}{dt}\right)_{CO_2}\Delta H_{CO_2}^{Gasif}, \tag{20}$$

where ΔH is the energy released due to heterogeneous reaction of the given species, α is the fraction of heat released to the gas and $1 - \alpha$ is the fraction of heat absorbed by the particle. In this study, $\alpha = 0.3$ was used. For all of the conditions explored in this work, the value of α has negligible impact on the predicted ignition delay since the devolatilization (not char oxidation) rate is the dominant factor determining the ignition delay. However, in situations where char oxidation becomes dominant, the value of α will play an important role. The source term in (20) includes the heat of char oxidation (exothermic) CO_2 and H_2O gasification (endothermic).

Finally, the source term appearing in the particle energy balance, (14), is written as

$$S_r = \frac{1-\alpha}{m_p C_p}\left(S_{p,CO}\Delta H_{CO} + S_{p,CO_2}\Delta H_{CO_2}\right)^{Oxid} + \frac{1-\alpha}{m_p C_p}\left(\frac{dm_c}{dt}\right)_{H_2O}^{Gasif}\Delta H_{H_2O}^{Gasif} + \frac{1-\alpha}{m_p C_p}\left(\frac{dm_c}{dt}\right)_{CO_2}^{Gasif}\Delta H_{CO_2}^{Gasif} + \frac{1}{m_p C_p}\left(S_{p,H_2O}\right)^{Evap}\lambda_{Evap}, \tag{21}$$

where ΔH is the enthalpy of reaction, λ_{Evap} is water's latent heat of vaporization and $(S_{p,H_2O})^{Evap}$ is defined in (28).

3. Chemical reaction models

3.1. Gas phase

Two models for the gas-phase chemistry were considered: detailed kinetics (Section 3.1.1) and infinitely fast (flame-sheet) chemistry (Section 3.1.2).

3.1.1. Full chemistry

The GRI3.0 mechanism, consisting of 53 species and 325 reaction is utilized [45]. Transport equations are solved for the species, with appropriate phase-exchange source terms for the devolatilization, vaporization, and char oxidation models.

3.1.2. Flame-sheet

The flame-sheet model assumes an infinitely fast reaction

$$r_i \rightarrow \pi_i, \tag{22}$$

where r_i and π_i are the moles of ith species (except O_2) in reactants and flame-sheet product, respectively. It is assumed that the products of reaction are CO_2, H_2O and N_2. The oxygen required to consume each species is defined as

$$\xi_i = (\sigma_{iC} + \sigma_{iH}/4 - \sigma_{iO}/2) \quad i \equiv \text{species, except } O_2, \tag{23}$$

where ξ_i represents stoichiometric oxygen to burn the one mole of species i and σ_{ik} is the number of element k in species i. The stoichiometric oxygen requirement (θ) can be calculated as

$$\theta = \sum_{i \neq O_2}^{n_s} r_i \xi_i. \tag{24}$$

The equivalence ratio, $\Phi = \frac{r_{O_2}}{\theta}$, is used to determine the products of reaction. In lean conditions ($\Phi \geq 1$),

$$\pi_i = \begin{cases} E_C^r & i = CO_2 \\ E_H^r/2 & i = H_2O \\ E_N^r/2 & i = N_2 \\ r_{O_2} - \theta & i = O_2 \\ 0 & \text{otherwise} \end{cases} \tag{25}$$

where $E_k^r = \sum_{i \neq O_2}^{n_s} r_i \sigma_{ik}$ is the amount of element k provided by the reactants.

Likewise, for rich conditions ($\Phi < 1$),

$$\pi_i = \begin{cases} r_{CO_2} + E_C^\pi & i = CO_2 \\ r_{H_2O} + E_H^\pi/2 & i = H_2O \\ r_{N_2} + E_N^\pi/2 & i = N_2 \\ 0 & i = O_2 \\ r_i(1 - \Phi \frac{\xi_i}{\sum_{l \neq O_2}^{n_s} \xi_l}) & \text{otherwise} \end{cases} \tag{26}$$

where

$$E_k^\pi = \Phi \sum_{i \neq O_2}^{n_s} r_i \sigma_{ik} \frac{\xi_i}{\sum_{l \neq O_2}^{n_s} \xi_l} \tag{27}$$

represents the number of moles of element k produced by reaction (22). In the flame-sheet model, transport equations are solved for each species that is involved in the coal models (devolatilization, vaporization and char oxidation) as well as any gaseous species fed into the reactor. The product composition is then obtained at each point in space and time using the methodology just discussed in this section.

3.2. Particle phase

In the proposed model, a coal particle consists of moisture, volatile, char and ash. Figure 1 depicts the coal's constituents and the models that describes mass exchange. For example, evaporation only adds moisture into the gas phase; however, char oxidation produces CO_2 and CO and consumes O_2. The models that describe the consumption of coal constituents are outlined in Sections 3.2.1, 2.2, 3.2.3.

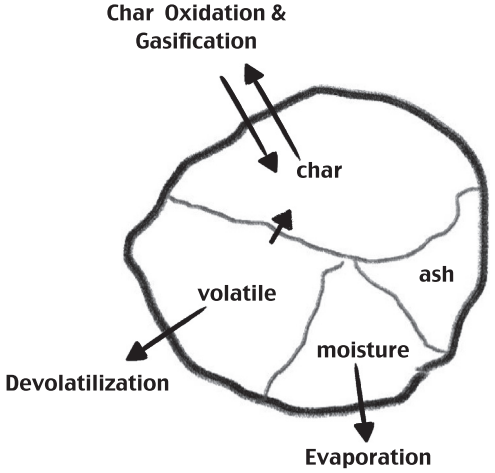

Fig. 1. Coal constituents.

3.2.1. Evaporation

The moisture content evolution is given by

$$\frac{dm_{H_2O}}{d}t = -(S_{p,H_2O})^{Evap} = k_v \left(\frac{P_{H_2O,sat}}{RT} - \frac{P_{H_2O}}{RT_g} \right) A_p M_{w,H_2O}, \tag{28}$$

where k_v is the mass transfer coefficient of steam into air [46], $P_{H_2O,sat}$ is the saturation pressure of water at particle temperature, P_{H_2O} is partial pressure of water in gas. For purposes of energy coupling, the latent heat of vaporization for water is calculated from the Watson relation [47,48], which provides the latent heat of vaporization as a function of temperature.

3.2.2. Devolatilization

Two devolatilization models with different complexity and computational cost were applied in this work.

3.2.2.1. Kobayashi–Sarofim model. The devolatilization rate described in this model has two weighted first order Arrhenius reaction rates [8],

$$\frac{dm_v}{dt} = -\left[\alpha_1 A_1 e^{(-E_1/RT_p)} + \alpha_2 A_2 e^{(-E_2/RT_p)} \right] m_v, \tag{29}$$

where α_1 and α_2 are weights of each rate [8] and the Arrhenius parameters (A_1, E_1, A_2, E_2) reported in [49] were used, consistent with several other studies [50–53]. The influence of the Arrhenius parameters for the Kobayashi–Sarofim model for coal simulations has been considered by [54]. Different reactions have been proposed for the Kobayashi devolatilization model [55]. Although there is no universally accepted form, in this work, we assume

$$CH_aO_b \rightarrow bCO + \frac{a+b-1}{2} H_2 + \frac{1-b}{2} C_2H_2, \tag{30}$$

where a and b are calculated from coal's ultimate and proximate analysis. There is general agreement on CO and H_2 as the products for Kobayashi model, but accounting for heavier species such as soot precursors and tar in the gas phase is less well-established. In this work, C_2H_2 represents heavy gas-phase species. The choice of C_2H_2 is motivated in part by its availability in GRI-3.0. However, results of ignition delay studies are relatively insensitive to this choice. Indeed, using CH_4 rather than C_2H_2 (with appropriate change in stoichiometry in (30)) resulted in almost no change in ignition delay. Thus, while the choice of heavy gas-phase species from the Kobayashi–Sarofim model may be critical for prediction of soot formation and tar evolution, its effect on ignition delay prediction is minimal.

3.2.2.2. Chemical Percolation Devolatilization (CPD) model. CPD is one of the most accurate (and complex) models available to predicts the production rates of the species during the devolatilization. CPD predicts the devolatilization of different coal types based on their chemical structure. In CPD, coal is described as a macromolecular network of aromatic ring clusters of various sizes and types that are connected by a variety of chemical bridges (so-called "labile bridges") of different bond strengths [13].

In this model, devolatilization starts with decomposing of labile bridges (l) to form highly reactive intermediate bridges (l^*). These intermediates further react to produce either char and light gases or side chains (δ) that may eventually convert into light gases. This process is represented schematically as

$$l \rightarrow l^* \begin{cases} \nearrow \delta \rightarrow \text{light gases} \\ \searrow \text{char} + \text{light gases} \end{cases}. \tag{31}$$

The CPD model employed herein involves solution of 18 ODEs on each particle to evolve the quantities related to devolatilization, and has been shown to provide accurate evolution of several light

gases for devolatilization of various coal types over a range of thermal conditions [15]. The gas-phase species produced by the CPD model are: CO_2, CO,CH_4, C_2H_2, HCN, NH_3, H and H_2O.

3.2.3. Char oxidation/gasification

Char oxidation and gasification represent heterogeneous reactions at the particle surface. The mass-exchange terms are accounted in the mass balance, (2). Char oxidation is a complex phenomenon which depends on many factors such as temperature and oxygen concentration. The rate of consumption of char by oxidation is described by [17]

$$\left(\frac{dm_c}{dt}\right)^{Oxid} = \frac{r_c M_{w,C}}{\varphi}\pi d_p^2, \tag{32}$$

where $\varphi = 2/(1+\psi)$ designates the stoichiometric ratio of carbon consumption, $M_{w,C}$ is the molecular weight of carbon and r_c is the reaction rate of char (33).

There are several models and equations that explain char oxidation reaction rate, the Langmuir–Hinshelwood is a kinetic expression that frequently used. This approach describes competing adsorption (O_2) and desorption (CO) on char surface that makes it more attractive. There are multiple forms for Langmuir–Hinshelwood, but it was shown by [17] that

$$r_c = \frac{k_2 k_1 P_{O_2,s}^{n_r}}{k_1 P_{O_2,s}^{n_r} + k_2}, \tag{33}$$

yields good results, where k_1 and k_2 are Arrhenius rate constants, $n_r = 0.3$ and $P_{O_2 s}$ is the partial pressure of oxygen at particle surface [17].

Char oxidation and gasification are heterogeneous reactions that consume char. The presence of carbon dioxide and water vapor around the coal particle increases the likelihood of gasification reactions at high temperatures through

$$C_{(s)} + CO_2 \longrightarrow 2CO, \tag{34}$$

$$C_{(s)} + H_2O \longrightarrow CO + H_2. \tag{35}$$

The differential equation describing char gasification is

$$\left(\frac{dm_c}{dt}\right)_i^{Gasif} = -k_i m_c; \quad i \equiv CO_2, H_2O, \tag{36}$$

where k_i is given by [56]

$$k_i = A_i P_i^{n_i} e^{-E_i/RT_p} \tag{37}$$

and P_i represents the partial pressure of CO_2 and H_2O around the particle for reactions (34) and (35), respectively. The Arrhenius rate parameters and reaction order (n_i) appearing in (37) are given by [57,56]. In this work, the evolution of particle surface area is accounted using a modified random pore model [58,59].

4. Computational configuration

This section briefly summarizes the computational parameters, models and configurations used for each simulation performed in this work. The computational configuration mirrors the experimental setup described in [25], which provides details such as particle size, coal feed rate, and gas phase conditions. The governing equations and models outlined in Section 2 are solved using a fully coupled, compressible algorithm with an explicit time integration scheme and a second-order finite volume spatial discretization. Characteristic boundary conditions are applied on the domain boundaries [60]. For the simulations reported herein, the computational domain is 1.4 cm with a grid spacing of 140 μm and time step of 2×10^{-8} s. The results are grid-converged; simulations performed on finer grids yield the same result for predicted ignition delay. A schematic of simulated system is illustrated in Fig. 2 where the one-dimensional domain oriented in the *y*-direction moves in *x*-direction via a space–time mapping using the mean system velocity [40]. The jet diameter is 0.75 mm and the particle position is aligned in the middle of the jet (system).

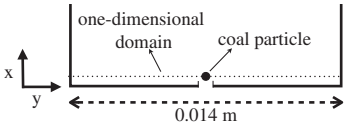

Fig. 2. A schematic of the simulated system.

In this work, two US coals are used: Pittsburgh high-volatile bituminous coal and Black Thunder subbituminous coal from the Powder River basin, with proximate and ultimate analysis reported by [25]. The coal particles are assumed to be spherical, with initial density of 1200 kg/m^3 and initial temperature of 298 K for all simulations.

The initial gas composition and temperature are uniform and constant over the computational domain, consistent with the experimental configuration described in [25]. Table 1 summarizes the key parameters varied as part of this work. The initial gas phase composition includes O_2, N_2, CO_2 and H_2O. The effect of O_2 composition is considered while maintaining the initial CO_2 and H_2O mole fractions constant at 0.3 and 0.116, respectively. Likewise, the initial streamwise velocity ($v = 2.5$ m/s) is uniform and constant over the domain, but evolves in time according to (3), with dilatational effects due to chemical reaction as well as particle vaporization, devolatilization and char oxidation accounted for. The coal particle has the same initial streamwise velocity as the gas phase. Cases *A*.1—*A*.8 each consider the effect of the initial gas phase temperature on the ignition delay, resulting in a number of distinct simulations being performed for each of these cases. Similarly, each case *B*.1—*B*.4 includes several simulations of particle sizes varying from 45-125 μm.

5. Result and discussion

Simulations were performed to investigate the effect of furnace temperature, particles size and coal type on ignition delay of coal particle. Furthermore, for particle and gas phase calculation, two methods with different levels of complexity and computation cost are utilized. To validate the simulation predictions, ignition delay as a metric is identified to compare the simulation results with experimental data.

Figure 3 shows the normalized volatile and char content of the coal particle for case *B*.1, and also indicates the location of ignition.[1] This figure suggests that ignition is characterized almost entirely by homogeneous gas-phase reactions rather than heterogeneous char reactions.

Figure 4 illustrates the spatio-temporal evolution of several fields for Case *B*.1 in Table 1 with a particle size of 92.4 μm. To show more detail on species evolution, the profiles of OH, CO and CH_4 at 30, 40 and 45 ms are illustrated in Fig. 5. During the first 25 ms, the gas phase temperature (Fig. 4(a)) decreases due to the cooler particle absorbing heat prior to the onset of ignition near 25 ms. The mass fraction of carbon monoxide (Y_{CO}) is illustrated in Fig. 4(b). Devolatilization produces CO as the particle heats up during $t = [0, 25]$ ms, with a spike in CO production around 25–

[1] Section 5.1 discusses the characterization of ignition in detail.

Table 1
Parameters for simulations considered herein.

Case	Coal type	Devolatilization model	Gas chemistry model	T_{gas} (K)	Particle size (μm)	O_2 (mole fraction)	N_2
A.1	Pittsburgh	CPD	Detailed kinetics	1200–1750	92.4	0.2	0.384
A.2	Pittsburgh	Kobayashi–Sarofim	Detailed kinetics	1200–1750	92.4	0.2	0.384
A.3	Pittsburgh	CPD	Flame-sheet	1200–1750	92.4	0.2	0.384
A.4	Pittsburgh	Kobayashi–Sarofim	Flame-sheet	1200–1750	92.4	0.2	0.384
A.5	Black Thunder	CPD	Detailed kinetics	1200–1750	92.4	0.2	0.384
A.6	Black Thunder	Kobayashi–Sarofim	Detailed kinetics	1200–1750	92.4	0.2	0.384
A.7	Black Thunder	CPD	Flame-sheet	1200–1750	92.4	0.2	0.384
A.8	Black Thunder	Kobayashi–Sarofim	Flame-sheet	1200–1750	92.4	0.2	0.384
B.1	Pittsburgh	CPD	Detailed kinetics	1320	45–125	0.12	0.464
B.2	Pittsburgh	Kobayashi–Sarofim	Detailed kinetics	1320	45–125	0.12	0.464
B.3	Pittsburgh	CPD	Flame-sheet	1320	45–125	0.12	0.464
B.4	Pittsburgh	Kobayashi–Sarofim	Flame-sheet	1320	45–125	0.12	0.464

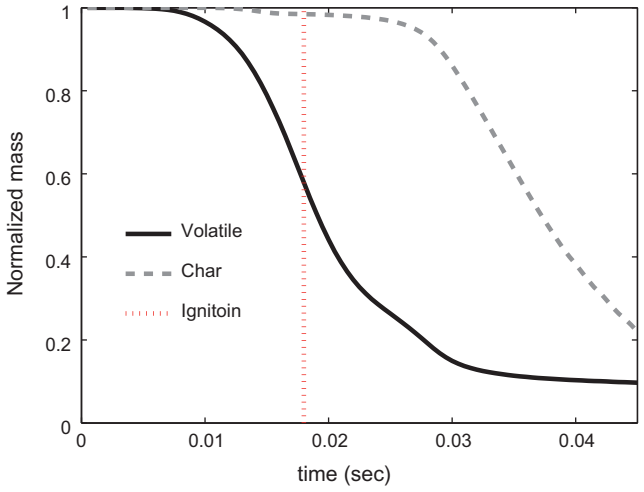

Fig. 3. Normalized volatile and char content in the coal particle as a function of time for case *B*.1.

30 ms as homogenous ignition occurs in the gas phase. After homogenous ignition, when the temperature of the particle and gas phase is high, char oxidation dominates CO production. Figure 4(c) shows the O_2 space–time evolution, which is consistent with the interpretation discussed in connection with the CO evolution. Gas phase (homogenous) reaction and char oxidation (heterogeneous) both contribute to the O_2 consumption, with homogenous reactions dominating initially and heterogeneous reactions dominating after homogeneous ignition. The evolution of OH, shown in Fig. 4(d), supports the observation that homogeneous ignition first occurs away from the particle surface, followed by heterogeneous char oxidation.

In Fig. 5 at time 30 ms OH has two local maxima (indicated by black arrows) and CH_4 has two corresponding maxima where homogenous reaction of volatiles begins. These maxima correspond to the two branches in Fig. 4(d) during $t \approx [27, 35]$ ms. By 40 ms, the released volatiles are consumed, as shown by Fig. 5(c) (here, CH_4 is chosen to represent the volatiles produced by the CPD model). The two local minima at 45 ms in the OH profile in

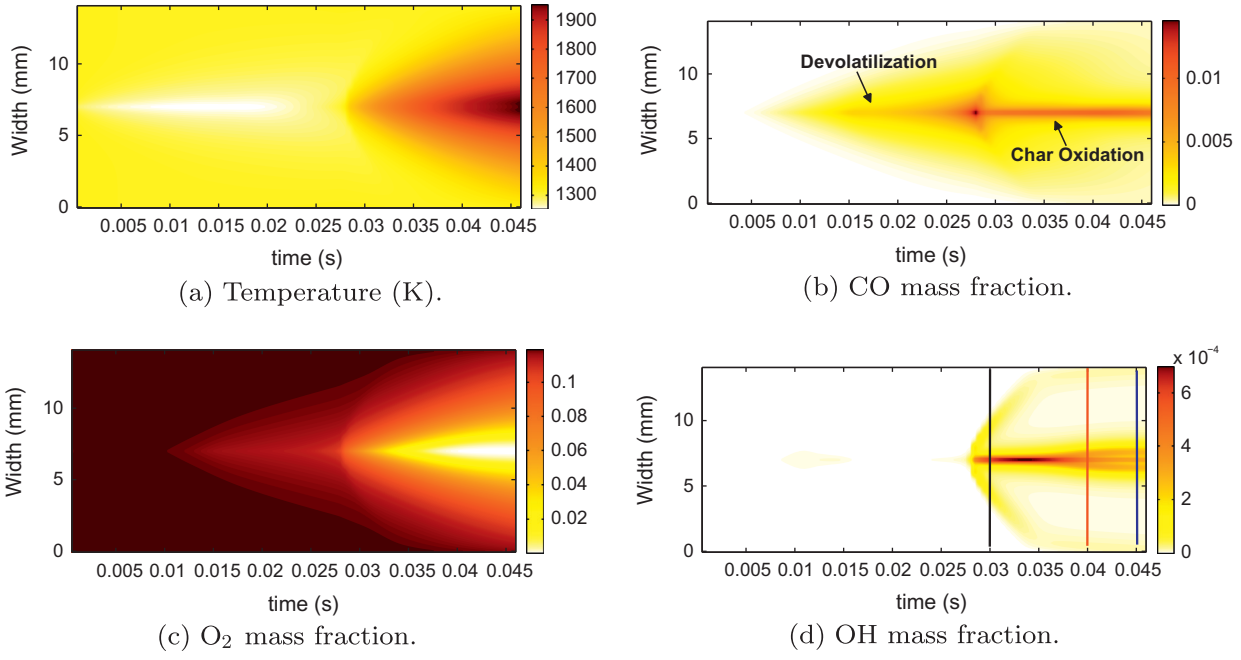

Fig. 4. Space–time evolution of several quantities associated with case *B*.1 (Table 1) with a 92.4-μm particle.

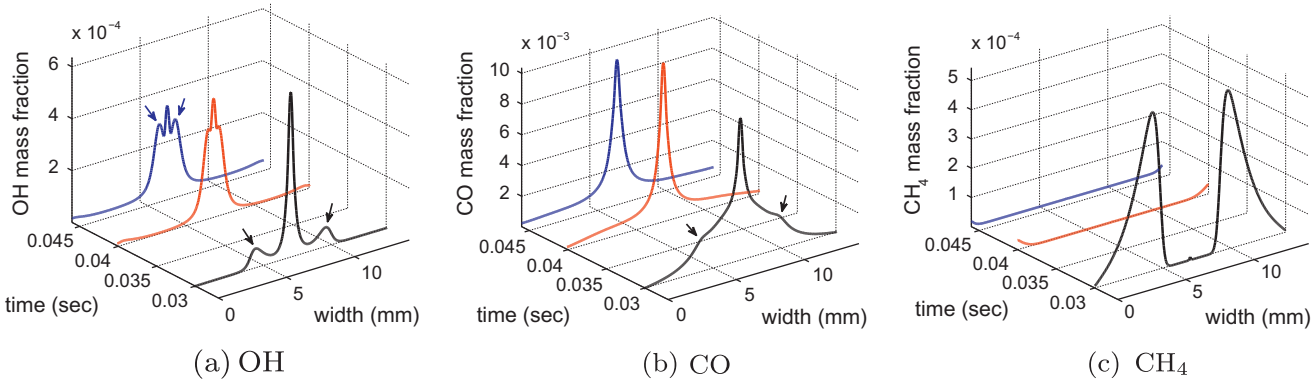

(a) OH (b) CO (c) CH_4

Fig. 5. Profiles of OH, CO and CH_4 at different times (30, 40 and 45 ms) for case *B*.1 (Table 1) with a 92.4-μm particle. Time slices correspond to the vertical lines shown in Fig. 4(d).

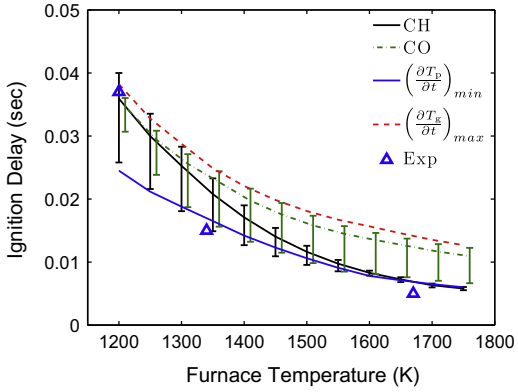

(a) Ignition delay for various criteria. Species criteria are based on the time at which the species mass fraction reaches half of its maximum. Experimental data are extracted from [25] .

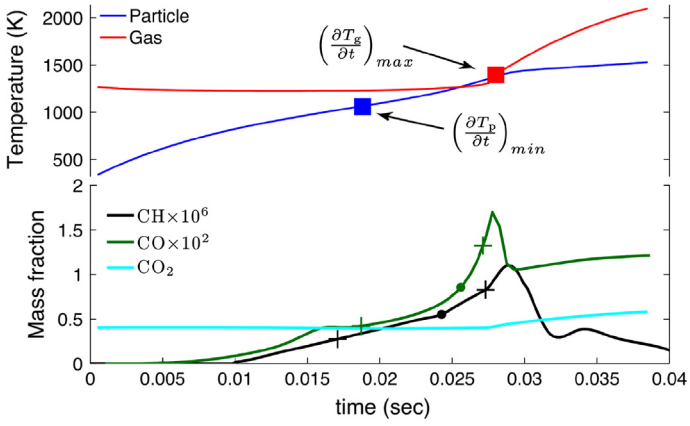

(b) Species (bottom) and particle temperature (top) histories. Crosses indicate 25% and 75% of the maximum species mass fraction and squares show the particle temperature inflection point $\left(\partial T_p/\partial t|_{min}\right)$ and the maximum gas-phase temperature increase rate $\left(\partial T_g/\partial t|_{max}\right)$.

Fig. 6. Ignition delay identified with half of maximum in species mass fraction profile. Pittsburgh coal particle with size of 92.4 μm injected into 20 vol% O_2 with N_2 diluent (Case *A*.1).

Fig. 5(a) (see the blue arrows)[2] correspond to the homogenous reactions with the byproducts (primarily CO) of char oxidation.

5.1. Ignition delay

In experiments, the most widely used methods to identify ignition delay are based on measurements of the intensity of visible light emission [61,25]. In the experimental results used in this work, CH^* emission is considered as an indicator of ignition, with the ignition point defined as the half of the CH^* maximum signal [25]. However, this signal was contaminated by CO_2^* and thermal radiation from hot soot and the coal/char particle [25].

Computationally, it is not obvious how to determine the ignition point. For example, threshold values of temperature or species mass fractions, or the inflection point in the particle temperature–time history (as suggested by [61]). Physically, the inflection point in the particle temperature history represents the location where the asymptotic heating of the particle by its surroundings is overtaken by the heat transfer due to chemical reaction nearby the particle.

Figure 6(a) shows the simulation prediction for ignition delay based on several plausible criteria. These results are for the same conditions as described in connection with Fig. 4, but with the inlet gas temperature varying. For the species criteria, ignition is defined as the time at which the species mass fraction is 50% of its maximum value. CO is chosen to be representative of the products of devolatilization and char oxidation and CH is chosen as a surrogate representation of CH^* which is the reported basis of the experimental measurements of ignition delay.

The bars in Fig. 6(a) represent 25% and 75% of the maximum mass fraction in the profiles of species, consistent with the approach taken in [25]. These "uncertainties" or sensitivities are not obtained through rigorous uncertainty or sensitivity analysis, as that is beyond the scope of this paper. Rather, they are provided to give an indication of the sensitivity of the reported ignition delay to the chosen definition. The time-evolution of these species and the particle temperature at the particle position are shown in Fig. 6(b). Since the ignition delay criteria based on CH provides the best agreement between the simulation and experimental data, it is used to identify the ignition delay in throughout the paper where detailed kinetics are utilized in the gas phase, unless specifically stated otherwise.

[2] For interpretation of color in Fig. 5, the reader is referred to the web version of this article.

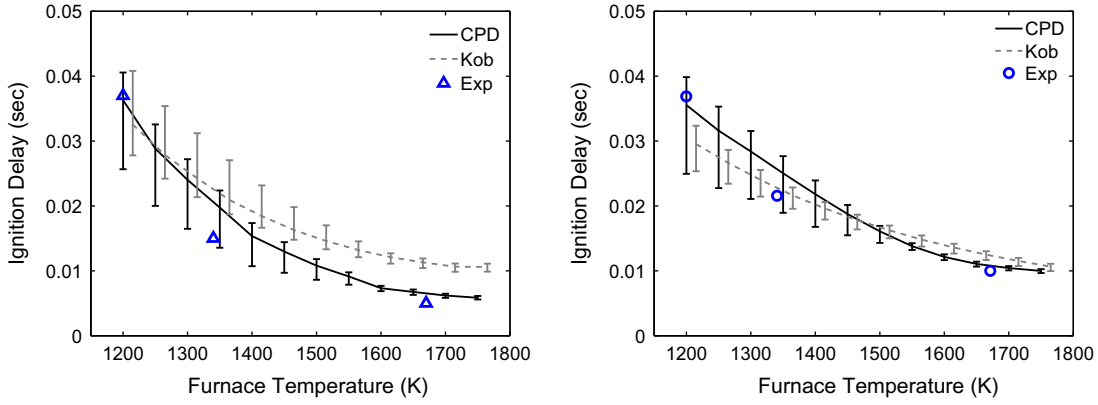

(a) Pittsburgh, cases $A.1$ & $A.2$ (b) BlackThunder, cases $A.5$ & $A.6$

Fig. 7. Ignition delay vs initial furnace temperature. 'CPD', 'Kob' and 'Exp' represent the CPD model, Kobayashi model and experimental data [25], respectively. Detailed kinetics in the gas phase was used.

The CH criteria is unavailable in flame-sheet method (discussed in Section 3.1.2) because intermediate species are not available. Therefore, CO and the particle temperature history inflection point as measures of ignition delay were used. As shown in Fig. 6, these are not expected to be highly accurate indicators of ignition delay, but provide a reasonable approximation. By assuming that the true ignition delay prediction for the flame-sheet method lays between the CO and particle inflection point, a comparison between detailed kinetics and flame-sheet can be made.

5.2. Effect of furnace temperature

Using the ignition delay criteria established in Section 5.1, the effect of furnace temperature on ignition delay for Pittsburgh and Black Thunder coals[3] is investigated. The simulation parameters and applied models for this study are give in Table 1 which includes cases $A.1$—$A.8$.

The experiments considered a particle size cut of 75-105 μm whereas the simulation adopts particles at the mass mean size of the size cut (92.4 μm). The model prediction of ignition delay as a function of particle size is considered in Section 5.3.

5.2.1. Detailed chemistry

Figure 7(a) shows the ignition delay as a function of furnace temperature for Pittsburgh (Fig. 7(a)) and Black Thunder (Fig. 7(b)) coals, respectively. Results for the CPD and Kobayashi models, both with detailed chemistry in the gas-phase, are compared with experimental data. Figure 7 indicates that the CDP model is more successful than Kobayashi model in predicting the ignition delay over the range of furnace temperatures and the two coal types, with larger discrepancies at higher furnace temperatures.

Figure 8 shows the particle temperature at ignition using the inflection point and CH_x criteria (see Section 5.1) with the CPD model and detailed chemistry in the gas phase, and indicates that ignition occurs at lower particle temperatures as the furnace temperature increases. Figure 8 also shows the results using the particle temperature inflection point criteria as an ignition definition, and demonstrates that the inflection point criterion results in significantly different particle temperatures at ignition. Furthermore, the sensitivity in particle temperature at ignition point is quite high at low furnace temperatures. All of this highlights the importance of carefully characterizing ignition, and also the potential difficulty of comparing computational and experimental data if simulations do not predict the same quantity being observed by the experiment.

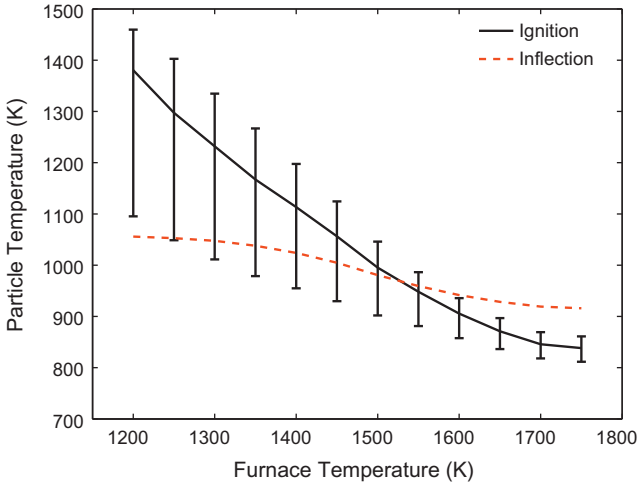

Fig. 8. Pittsburgh coal particle temperature at ignition and inflection point by utilizing CPD model (case $A.1$). Ignition is characterized by half of CH_x maximum. Vertical bars show 25% and 75% of maximum.

The volatile consumption fractions at the ignition point for both devolatilization models are reported in Fig. 9. The CPD model shows a much more pronounced effect of the furnace temperature on the volatile consumption fraction at ignition. As a consequence of producing highly reactive species such as H, the consumption fraction of CPD model at high temperature is lower than the Kobayashi model. The particle temperature at ignition point decreases as initial furnace temperature increases in Fig. 8, which can be explained by the fact that less volatile is required for ignition as furnace temperature increases.

5.2.2. Flame-sheet model

We now consider the flame-sheet model for the gas-phase chemistry treatment. As a very inexpensive model, this is attractive for use in large-scale simulations, provided that it is sufficiently accurate. As discussed in Section 5.1, the CO profile at particle position and inflection point in particle temperature history are used to identify the ignition point since the flame-sheet model does not provide CH_x radical species for comparison with the experimental measurements.

[3] The proximate and ultimate analysis for these coals was taken from [25].

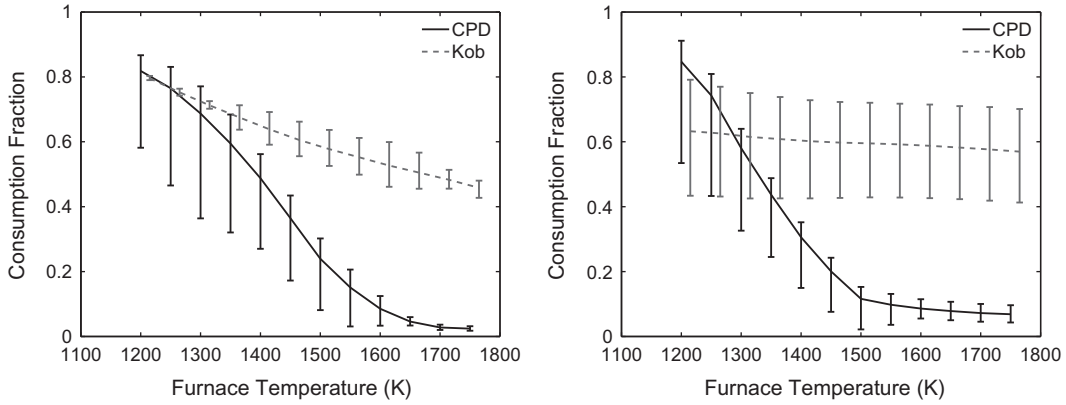

(a) Pittsburgh, cases $A.1$ & $A.2$ (b) Black Thunder, cases $A.5$ & $A.6$

Fig. 9. Volatile consumption fraction versus initial furnace temperature. 'CPD' and 'Kob' represent the CPD and Kobayashi models, respectively.

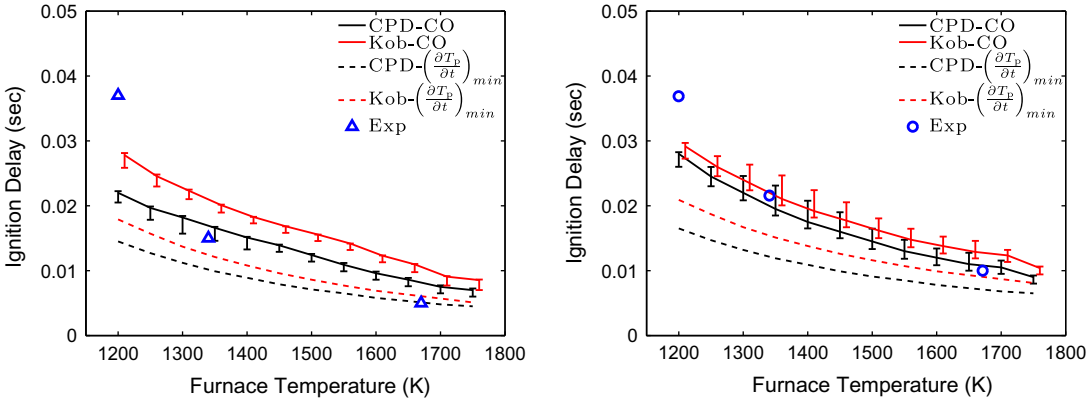

(a) Pittsburgh, cases $A.3$ & $A.4$ (b) Black Thunder, cases $A.7$ & $A.8$

Fig. 10. Ignition delay vs initial furnace temperature. 'CPD', 'Kob' and 'Exp' refer to the CPD model, the Kobayashi model and experimental data [25], respectively. These results employ the flame-sheet calculation in the gas phase.

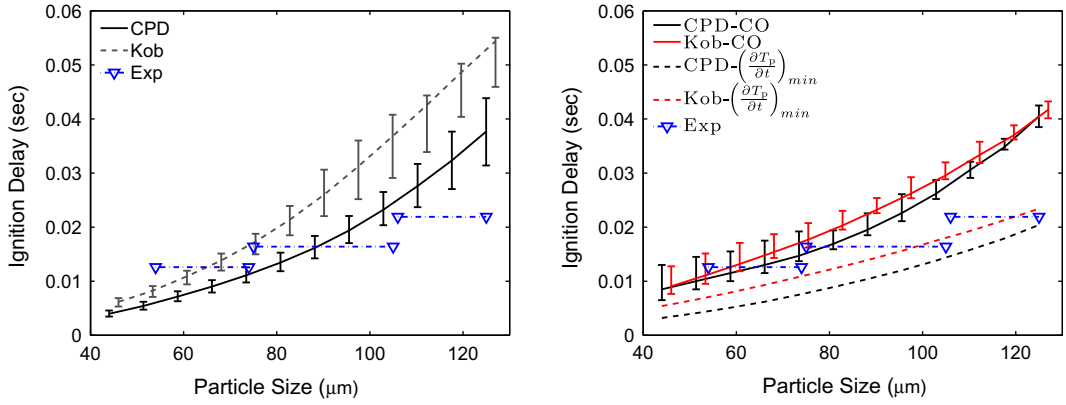

(a) Detailed kinetics, cases $B.1$ & $B.2$ (b) Flame-sheet chemistry, cases $B.3$ & $B.4$

Fig. 11. Ignition delay versus particle size for a Pittsburgh coal particle injected into 12 vol% O_2 in N_2 at 1320 K. The experimental data are shown for the three particle size cuts used experimentally.

Figure 10 shows the ignition delay as a function of furnace temperature, analogous to the results shown in Fig. 7 for detailed gas-phase chemistry. The difference between the CPD and Kobayashi models is not as pronounced when flame-sheet chemistry is used in the gas phase as when detailed kinetics are used (see Fig. 6(a)). Overall, the flame-sheet model paired with either devolatilization model does not perform as well as the detailed chemistry treatment paired with the CPD model, and fails to capture the nonlinear trend of ignition delay versus furnace temperature that the data shows. Some of this discrepancy can be attributed to the lack of a suitable metric for ignition delay with the flame-sheet model, as discussed in Section 5.1.

5.3. Particle size effects

The experimental data were obtained on particle sizes in different ranges [25], giving some uncertainty as to the effect of particle size variation within the cut on the resulting ignition delay. The effect of particle size on ignition delay for an initial furnace temperature of 1320 K is illustrated in Fig. 11. The triangles connected by dash-dot lines indicate experimentally measured ignition delay for the three different particle size cuts used in the experiments [25]. Also shown are the computational results for particles of different sizes.

Figure 11(a) compares experimental data to results for the CPD and Kobayashi models with detailed gas-phase chemistry (cases *B*.1 and *B*.2 in Table 1). The models show a larger effect of particle size on ignition delay than is observed experimentally. Nevertheless, the CPD model with detailed gas-phase chemistry does compare more favorably with the experimental data than the Kobayashi model. For comparison, the ignition delay trends using the flame-sheet model (cases *B*.3 and *B*.4 in Table 1) are shown in Fig. 11(b). Consistent with results discussed in Section 5.2.2, the flame-sheet model paired with either of the devolatilization models is not as accurate as the detailed kinetic model paired with CPD.

6. Conclusions

This paper considered several models for coal particle ignition and compared these to experimental measurements available in the literature for two coal types at various furnace temperatures and for several particle sizes. Two models for devolatilization (CPD and the Kobayashi–Sarofim model) and two for the gas phase chemistry treatment (detailed kinetics and a flame-sheet model) were applied. These models essentially trade complexity for cost.

To the authors' knowledge, this is the first simulation performed using detailed kinetics in the gas phase fully coupled to a high-fidelity model (CPD) for devolatilization of coal particles. The CPD model attempts to predict the light-gas evolution for the coal particles.

The results indicate that simpler Kobayashi–Sarofim and flame-sheet models roughly capture general trends present in the experimental data, but fail to provide quantitative agreement. On the other hand, the CPD model paired with detailed gas-phase chemistry provides reasonable agreement with the experimental observations over all reported conditions. This suggests that detailed devolatilization and gas-phase chemistry modeling are important to provide accurate characterization of ignition delay. This conclusion also applies when considering the ability of the models to capture trends when varying furnace temperature and particle size.

The amount of volatile produced by each devolatilization model at ignition is compared, and varies significantly between the CPD and Kobayashi–Sarofim models, with the CPD model showing much more sensitivity to the gas phase temperature in predicting the volatile yield at the point of ignition.

One significant challenge in comparing to experimental data is determining how to define ignition in the simulation. This is particularly challenging for the flame-sheet model where intermediate species are unavailable for comparison against the emission measurements of CH^* in the experiment. A rough indication of the sensitivity of the model predictions to the definition of the ignition delay are also presented.

Acknowledgments

This material is based upon work supported by the Department of Energy under Award Number DE-NT0005015. The views and opinions of authors expressed herein do not necessarily state or reflect those of the United States government or any agency thereof.

References

[1] K.L. Smith, L.D. Smoot, T.H. Fletcher, R.J. Pugmire, The Structure and Reaction Process of Coal, Plenum Press, New York, 1994.
[2] W. Eisermann, P. Johnson, W. Conger, Fuel Process. Technol. 3 (1980) 39–53.
[3] R.E. Mitchell, L. Ma, B. Kim, Combust. Flame 151 (2007) 426–436.
[4] F.Y. Wang, S.K. Bhatia, Chem. Eng. Sci. 56 (2001) 3683–3697.
[5] R.C. Shurtz, K.K. Kolste, T.H. Fletcher, Energy Fuels 25 (2011) 2163–2173.
[6] M.M. Baum, P.J. Street, Combust. Sci. Technol. 3 (1971) 231–243.
[7] S. Badzioch, P.G.W. Hawksley, Ind. Eng. Chem. Process Des. Develop. 9 (4) (1970) 521–530.
[8] H. Kobayashi, J.B. Howard, A.F. Sarofim, Symp. (Int.) Combust. 16 (1977) 411–425.
[9] D.B. Anthony, J.B. Howard, AICHE J. 22 (4) (1976) 625–656.
[10] C.P. Please, M.J. McGuinness, D.L.S. McElwain, Combust. Flame 133 (2003) 107–117.
[11] G.R. Gavalas, P.H.-K. Cheong, R. Jain, Ind. Eng. Chem. Fundam. 20 (2) (1981) 113–122.
[12] P.R. Solomon, D.G. Hamblen, R.M. Carangelo, M.A. Serio, G.V. Deshpande, Energy Fuels 2 (1988) 405–422.
[13] D.M. Grant, R.J. Pugmire, T.H. Fletcher, A.R. Kerstein, Energy Fuels 3 (1989) 175–186. <http://pubs.acs.org/doi/pdf/10.1021/ef00014a011>.
[14] B.S. Brewster, L.L. Baxter, L.D. Smoot, Energy Fuels 2 (1988) 362–370.
[15] R.S. Jupudi, V. Zamansky, T.H. Fletcher, Energy Fuels 23 (2009) 3063–3067.
[16] I.W. Smith, Symp. (Int.) Combust. 19 (1982) 1045–1065.
[17] J.J. Murphy, C.R. Shaddix, Combust. Flame 144 (4) (2006) 710–729.
[18] L. Ma, R. Mitchell, Combust. Flame 156 (1) (2009) 37–50.
[19] R.E. Mitchell, Symp. (Int.) Combust. 22 (1) (1988) 69–78.
[20] L. Tognotti, J.P. Longwell, A.F. Sarofim, Symp. (Int.) Combust. 23 (1) (1991) 1207–1213.
[21] M. Vascellari, G. Cau, Fuel 101 (2012) 90–101.
[22] M. Vascellari, R. Arora, M. Pollack, C. Hasse, Fuel 113 (2013) 654–669.
[23] Y.A. Levendis, K. Joshi, R. Khatami, A.F. Sarofim, Combust. Flame 158 (2011) 452–465.
[24] T. Maffei, R. Khatami, S. Pierucci, T. Faravelli, E. Ranzi, Y.A. Levendis, Combust. Flame 160 (2013) 2559–2572.
[25] Y. Liu, M. Geier, A. Molina, C.R. Shaddix, Int. J. Greenhouse Gas Contr. 5 (2011) S36–S46.
[26] R. Jovanovic, B. Rašuo, P. Stefanovic, D. Cvetinovic, B. Swiatkowski, Int. J. Heat Mass Transfer 58 (2013) 654–663.
[27] R. Khatami, C. Stivers, K. Joshi, Y.A. Levendis, A.F. Sarofim, Combustion behavior of single particles from three different coal ranks and from sugar cane bagasse in O2/N2 and O2/CO2 atmospheres, Combustion and Flame 159 (1253-1271).
[28] R. Khatami, C. Stivers, Y.A. Levendis, Combust. Flame 159 (2012) 3554–3568.
[29] A. Ponzio, S. Senthoorselvan, W. Yang, W. Blasiak, O. Eriksson, Fuel 87 (2008) 974–987.
[30] L. Chen, S.Z. Yong, A.F. Ghoniem, Prog. Energy Combust. Sci. 38 (2012) 156–214.
[31] M. Vascellari, C.H.H. Xu, Proc. Combust. Inst. 34 (2013) 2445–2452.
[32] F. Higuera, Combust. Flame 156 (2009) 1023–1034.
[33] M. Zhu, H. Zhang, Z. Zhang, D. Zhang, Combust. Sci. Technol. 183 (11) (2011) 1221–1235.
[34] C.W. Lau, S. Niksa, Combust. Flame 90 (1) (1992) 45–70.
[35] C. Wang, G. Berry, K. Chang, A. Wolsky, Combust. Flame 72 (3) (1988) 301–310.
[36] M. Jost, I. Leslie, C. Kruger, Proc. Combust. Inst. 20 (1) (1985) 1531–1537.
[37] E.S. Hecht, C.R. Shaddix, A. Molina, B.S. Haynes, Proc. Combust. Inst. 33 (2011) 1699–1706.
[38] E.S. Hecht, C.R. Shaddix, M. Geier, A. Molina, B.S. Haynes, Combust. Flame 159 (2012) 3437–3447.
[39] E.S. Hecht, C.R. Shaddix, J.S. Lighty, Combust. Flame 160 (2013) 1499–1509.
[40] J.C. Sutherland, N. Punati, A.R. Kerstein, Inst. Clean Secure Energy (2010).
[41] A.R. Kerstein, J. Fluid Mech. 392 (1999) 277–334.
[42] N. Punati, An Eulerian One-Dimensional Turbulence Model: Application to Turbulent and Multiphase Reacting Flows, Ph.D. thesis, Department of Chemical Engineering, University of Utah, January 2012.
[43] F.P. Incropera, D.P. DeWitt, Introduction to Heat Transfer, fourth ed., John Wiley & Sons, 2002.
[44] C.T. Crowe, J.D. Schwarzkodf, M. Sommerfeld, Y. Tsuji, Multiphase Flows with Droplets and Particles, second ed., CRC Press, 2012.
[45] N. Slavinskaya, M. Braun-Unkhoff, P. Frank, Inst. Combust. Technol. 130 (2008) 38–40.
[46] G. Nellis, S. Klein, Heat Transfer, Cambridge, 2008.
[47] B.E. Poling, J.M. Prausnitz, J.P. O'Connell, The Properties of Gases and Liquids, fifth ed., McGraw-Hill, 2004.
[48] K.M. Watson, Ind. Eng. Chem. 35 (4) (1943) 398–406.
[49] S.K. Ubhayakar, D.B. Stickler, C.W. Von Rosenberg Jr., R.E. Gannon, Symp. (Int.) Combust. 16 (1) (1977) 427–436.
[50] Y.S. Shen, B.Y. Guo, A.B. Yu, P. Zulli, Fuel 88 (2009) 255–263.
[51] C. Chena, M. Horioa, T. Kojimab, Fuel 80 (2001) 1513–1523.

[52] E.G. Eddings, A. Molina, D.W. Pershing, A.F. Sarofim, T.H. Fletcher, H. Zhang, K.A. Davis, M. Denison, H. Shim, Minimization of NO Emissions from Multi-Burner Coal-Fired Boilers, Tech. Rep., U.S. Dept. of Energy, 2002.
[53] J. Pedel, J.N. Thornock, P.J. Smith, Combust. Flame 160 (2013) 1112–1128.
[54] N. Hashimoto, R. Kurose, S.-M. Hwang, H. Tsuji, H. Shirai, Combust. Flame 159 (2012) 353–366.
[55] A. Silaen, T. Wang, Int. J. Heat Mass Transfer 53 (2010) 2074–2091.
[56] H. Watanabe, M. Otaka, Fuel 85 (2006) 1935–1943.
[57] S. Kajitani, S. Hara, H. Matsuda, Fuel 81 (5) (2002) 539–546.
[58] H. Liu, C. Luo, M. Kaneko, S. Kato, T. Kojima, Energy Fuels 17 (2003) 961–970.
[59] T. Morimoto, T. Ochiai, S. Wasaka, H. Oda, Energy Fuels 20 (2006) 353–358.
[60] J.C. Sutherland, C.A. Kennedy, J. Comput. Phys. 191 (2) (2003) 502–524.
[61] R. Jovanovic, A. Milewska, B. Swiatkowski, A. Goanta, H. Spliethoff, Int. J. Heat Mass Transfer 54 (4) (2011) 921–931.

Please cite this article in press as: B. Goshayeshi, J.C. Sutherland, Combust. Flame (2014), http://dx.doi.org/10.1016/j.combustflame.2014.01.010